Phonon-mediated Superconductivity in Magic-strain Bilayer Graphene

Qingxiang Ji[1†], Bohan Li[1†], Johan Christensen[2], Changguo Wang[1*], Muamer Kadic[3*]

[1]National Key Laboratory of Science and Technology on Advanced Composites in Special Environments, Harbin Institute of Technology, Harbin, 150001, PR China
[2] IMDEA Materials Institute, Calle Eric Kandel 2 28906, Getafe (Madrid), Spain
[3]Université Marie et Louis Pasteur, Institut FEMTO-ST, CNRS, 25000 Besançon, France
† These authors contributed equally to this work.
*Corresponding authors. E-mail: wangcg@hit.edu.cn; muamer.kadic@femto-st.fr

Extensive investigations on the Moiré magic-angle have been conducted in twisted bilayer graphene, unlocking the mystery of unconventional superconductivity and insulating states. In analog to magic angle, here we demonstrate the new concept of magic-strain in graphene systems by judiciously tailoring mechanical relaxation (stretch and compression) which is easier to implement in practice. We elucidate the interplay of strain-induced effects and delve into the resulting unconventional superconductivity or semimetal-insulator transition in relaxation-strained graphene, going beyond the traditional twisting approach. Our findings reveal how relaxation strain can trigger superconducting transitions (with an ultra-flat band at the Fermi level) or the semimetal-insulator transition (with a gap opening at the K point of 0.39 eV) in both monolayer and bilayer graphene. These discoveries open up a new branch for correlated phenomena and provide deeper insights into the underlying physics of superconductors, which positions graphene as a highly tunable platform for novel electronic applications.

Keywords:Magic-strain, Superconductivity, Graphene, Tight-binding model

Introduction

Functional materials are engineered materials designed with specific functionalities in mind. They play a crucial role in various technological advancements to harness sound [1, 2, 3], light [4], vibrations [5], heat [6, 7] and electronic states [8, 9]. For many years, classical metamaterials have been the workhorse of the functional materials field. By manipulating their artificial structure features at the subwavelength scale, metamaterials achieve an array of exotic properties not found in natural materials [10]. For instance, metamaterials can bend light or sound in unusual ways, create invisibility cloaks, or possess negative refractive index [11, 12].

In recent years, a new class of functional materials has emerged – Van der Waals (vdW) metamaterials. As the name suggests, vdW metamaterials are the marriage of vdW materials and metamaterial design principles. They create intricate heterostructures by stacking different vdW materials. These heterostructures can be tailored to exhibit entirely new properties due to the combined effects of their individual components [13, 14, 15], opening doors to novel functionalities not achievable by classical metamaterials alone. The vdW metamaterials have shown great potential as tunable correlated electron systems, and have demonstrated various intriguing properties by varying the stacking configuration of low-dimension material sheets, e.g., graphene and Mexenes [16, 17, 18, 19, 20]. For graphene, the emergent heterostructures have added them a long list of miraculous properties such as the superconducting and insulating state. Compared to other superconducting materials with intense doping [21], e.g., copper oxide [22], iron-based [23] and MgB_2 superconductors [24], graphene has unique advantages of being a single-atomic lattice structure. This superlattice characteristic expands possibilities to tune graphene's conductivity properties by tailoring its heterostructure using mechanical deformation/strain. Strain is an effective way for engineering flat bands that favor the emergence of superconductivity or other correlated phases [25, 26, 27, 28, 29, 30, 31, 32, 33]. Recently experiments have demonstrated superconducting states in twisted bilayer graphene (TBG) [34]. Superconductivity of twisted graphene systems is rooted in Moiré-modulation of the interlayer coupling,

which is depicted by Dirac models that flatten the electronic bands at particular angles [35, 36]. The fascinating physics of correlated graphene Moiré superlattices, such as TBG, has generated extensive efforts to uncover the mysteries of their phase diagrams [37]. As a typical example, the independent-layer behavior and the reduction of the Fermi velocity are observed for small angles in TBG. Specifically, when the torsional angle is close to 1.1° (magic angle), superconductivity and Mott insulator behavior can be induced in TBG. In addition, magic angles can also cause some exotic phenomena in optics and mechanics [38, 39]. So far, an outburst of research has been conducted on twisting modulation. However, accurate twisting is laborious and needs intense efforts during sample fabrication. The influence of in-plane stain/deformation generated during the twisting process is also neglected [40, 41, 42].

Compared with twisting, relaxation (stretch or compression), which is widely adopted in mechanics, is easier to implement and holds potential for large-scale device applications. Researchers demonstrate that modulating relaxation strain can generate an approximate flat-band state or induce a bandgap in monolayer graphene, similar to those produced in twisted bilayer configurations. Experiments that engineer relaxation strain on graphene membranes have reported unexpected electronic transport and peculiar local density of states features [43, 44]. Although intriguing phenomena have been predicted, there is a gap in connecting the unconventional properties to distinct strain behavior. Knowledge of the strain features that determine the resulting electronic properties is highly desirable. Currently various strain conditions have been implemented in monolayer graphene, but the bandgap tunability is relatively confined. For bilayer graphene, the strain effects are studied all within the framework of twisted conditions [45, 46, 47]. We note that the using bi-axial relaxation strain on graphene systems (monolayer and bilayer) to achieve unconventional properties, which is predicted to have a higher degree of tunability (meanwhile more complicated), remains elusive. Consequently, the potential of relaxation-strained graphene to tailor electronic properties remains untapped.

In this work, we address these issues by developing tight-binding models that control bi-axial strain on graphene sheets. Firstly, we study monolayer graphenes with symmetrical strain distribution and demonstrate that relaxation will influence the Fermi velocity near the K point. Based on this finding, we adopt a general deformation manner where the graphene is stretched in one direction and compressed in the perpendicular direction. This technique allows us to open the bandgap largely (0.39 eV) and generate a semimetal-insulator transition for monolayer graphene. Then we turn to investigate Bernal-stacked graphene and reveal the relationship between interlayer distance and weak Van der Waals force for bilayer graphene systems. By fixing one graphene layer and stretching another layer with a symmetrical strain rate of 1.9% (magic strain), we display unambiguously a flat band at the Fermi level, indicating a superconducting transition. In addition, the asymmetric strain on bilayer graphene will open the bandgap with small margins (0.0272 eV), much less than the monolayer counterpart (0.39 eV).

Material and methods

We construct a tight-binding model (TBM) for monolayer graphene sheets, based on which we investigate the band structure considering two types of strain distributions:

(i) symmetrical strain distribution which retains hexagonal symmetry and is defined as $\varepsilon_{\mathrm{H}} = (a - a_0)/a_0$. The terms a and a_0 denote the lattice parameters before and after deformation, respectively (Figure 1a);

(ii) asymmetrical strain distribution along $x-$ (or $y-$) direction which corresponds to strain parallel to the zigzag (or armchair) edge of graphene ribbons and is defined as $\varepsilon_x = (L_{x1} - L_x)/L_x$ (or $\varepsilon_y = (L_{y1} - L_y)/L_y$) and $\varepsilon_x \neq \varepsilon_y$. Here L_x (L_{x1}) and L_y (L_{y1}) are the half diagonal lengths of the pristine (deformed) cells (Figure 1b).

We first establish the TBM for symmetrical strained monolayer graphene only considering on-site and nearest-neighbor hopping, as shown in Figure 1a. The Hamiltonian for monolayer graphene can be expressed as

$$H = -t \sum_{\boldsymbol{R}} c_A^{\dagger}(\boldsymbol{R}) \left(c_A(\boldsymbol{R}) + c_B(\boldsymbol{R} - \boldsymbol{a}_1) + c_B(\boldsymbol{R} - \boldsymbol{a}_2) \right) + h.c., \tag{1}$$

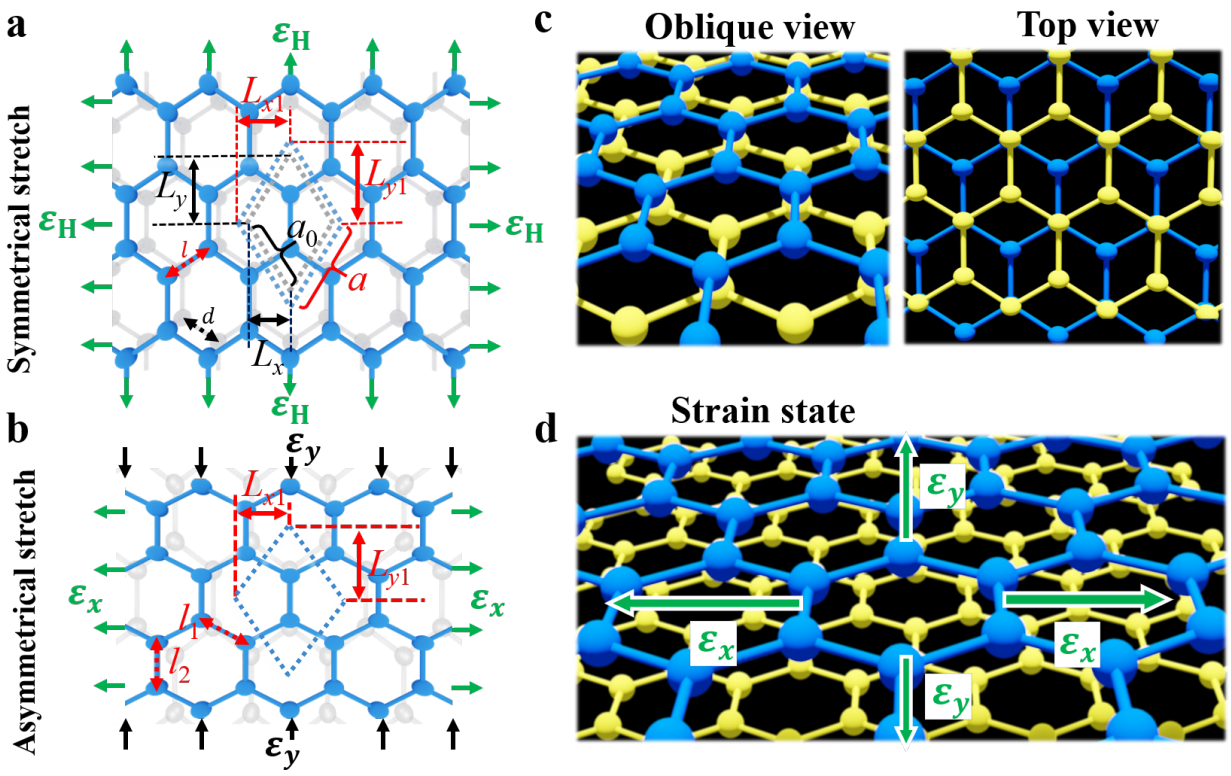

Figure 1: Relaxation-strain of monolayer graphene with **(a)** symmetrical deformation ($\varepsilon_x = \varepsilon_y = \varepsilon_H$) and **(b)** asymmetrical deformation along x and y directions ($\varepsilon_x \neq \varepsilon_y$). Here, the graphene in white (blue) is pristine (deformed), L_x (L_{x_1}) and L_y (L_{y_1}) are the half diagonal lengths of the pristine (deformed) cells, respectively. Diagram of **(c)** pristine and **(d)** deformed bilayer graphene are also depicted.

where $c_A^\dagger(\boldsymbol{R})$ and $c_A(\boldsymbol{R})$ are creation (annihilation) operators for an electron in an atomic-like state of kind A (i.e., three adjacent carbon atoms forms a regular triangle). The terms $\boldsymbol{a}_1$ and $\boldsymbol{a}_2$ are basis vectors for the unit cell, $\boldsymbol{R}$ is the position of the unit cell, and $h.c.$ stands for hermitian conjugate. We obtain the Hamiltonian for symmetrical strained monolayer graphene $H_{\mathrm{SMG}}(\boldsymbol{k})$ by

$$H_{\mathrm{SMG}}(\boldsymbol{k}) = \begin{bmatrix} 0 & -tf(\boldsymbol{k}) \\ -tf^*(\boldsymbol{k}) & 0 \end{bmatrix}, \tag{2}$$

where we have $f(\boldsymbol{k}) = \sum_{i=1}^{3} e^{i\boldsymbol{k}\cdot\boldsymbol{d}_i}$ and $\boldsymbol{d}_1$ = ($\boldsymbol{a}_1$ + $\boldsymbol{a}_2$)(1 + ε_H)/3, $\boldsymbol{d}_2$ = (-2$\boldsymbol{a}_1$ + $\boldsymbol{a}_2$)(1 + ε_H)/3, $\boldsymbol{d}_3$ = ($\boldsymbol{a}_1$-2$\boldsymbol{a}_2$)(1 + ε_H)/3. After imposing symmetrical strain distributions, the hopping parameters t with the bond length is expressed as $V_{pp\pi}(l) = t_0 e^{-3.37(l/d-1)}$, where d is the c-c bond length for undeformed graphene [48, 49].

For asymmetrical strained monolayer graphene (Figure 1b), the Hamiltonian changes its form to

$$H_{\mathrm{ASMG}}(\boldsymbol{k}) = \begin{bmatrix} 0 & -(t_2 - t_1) - t_1 f(\boldsymbol{k}) \\ (-t_2 - t_1) - t_1 f^*(\boldsymbol{k}) & 0 \end{bmatrix}, \tag{3}$$

where the new added terms $t_1 = V_{pp\pi}(l_1)$ and $t_2 = V_{pp\pi}(l_2)$ denote the hopping parameters.

We then move to construct TBM of bilayer graphene considering only a homogeneous interlayer hopping between the nearest neighbors, as shown in Figure 1c. The Hamiltonian can be written as the sum of the following terms

$$H = H_1 + H_2 + \langle 1, \boldsymbol{R}, A | H_\perp | 2, \boldsymbol{R}, B \rangle \sum_{\boldsymbol{R}} c_{1,A}^\dagger(\boldsymbol{R}) c_{2,B}(\boldsymbol{R}) + h.c., \tag{4}$$

where H_1 and H_2 are the Hamiltonian for each monolayer graphene, while $H_\perp$ indicates Hamiltonian interlayer coupling in the second quantized formalism. The Hamiltonian $H_{\mathrm{BLG}}(\boldsymbol{k})$ of Bernal-stacked bilayer

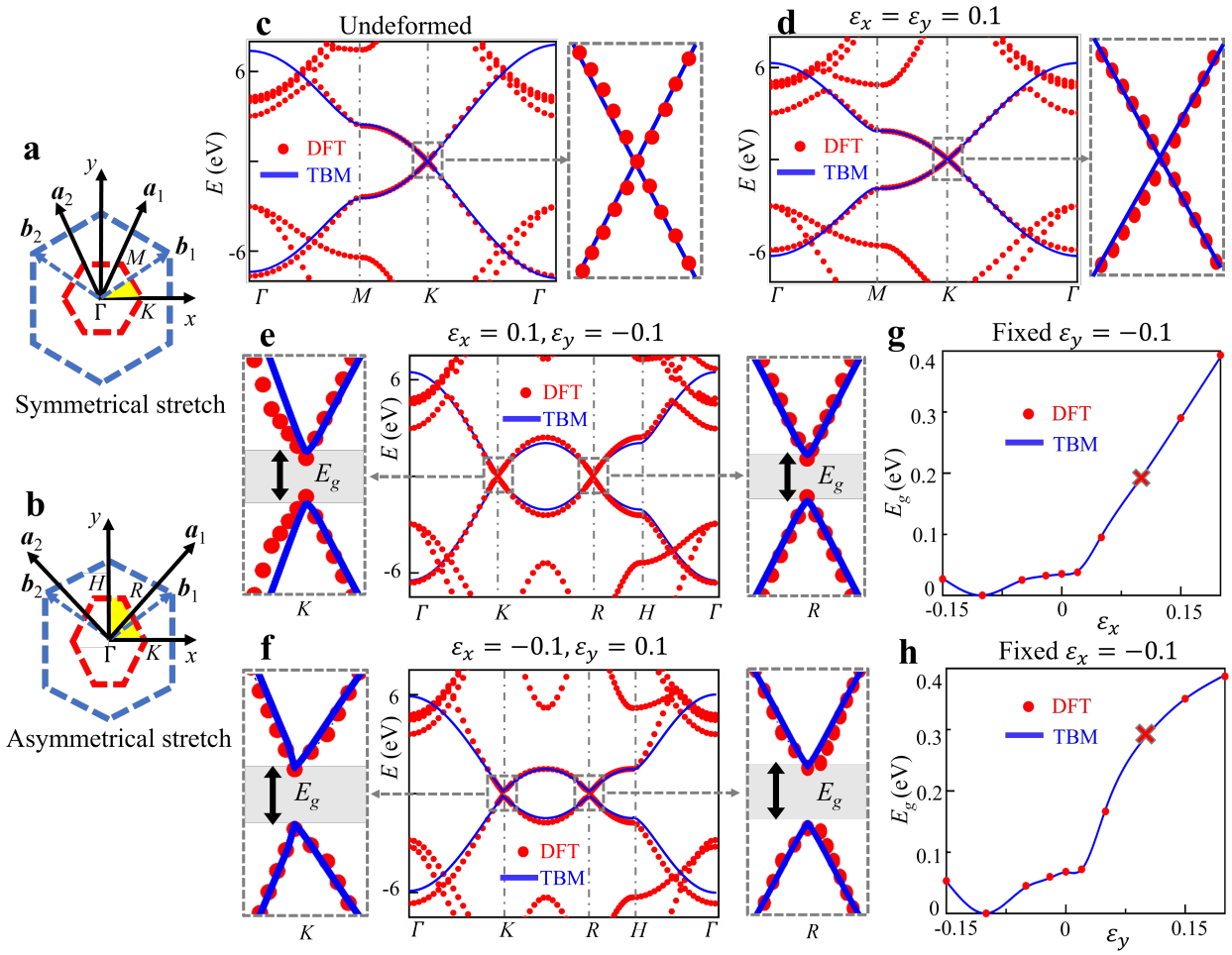

Figure 2: Semimetal-insulator transition for monolayer graphene. Irreducible Brillouin zones (in yellow) are shown for monolayer graphene under **(a)** symmetrical and **(b)** asymmetrical stretching. Reciprocal lattices (in navy dashed lines) and Brillouin zones (in red dashed lines) are depicted for clarity. Band structures of monolayer graphene are obtained by TBM (by blue solid lines) and DFT (by red dots) methods considering **(c)** pristine; **(d)** symmetrical strain and **(e, f)** asymmetrical strain, respectively. The zooms show that bandgaps E_g are generated only in asymmetrical strain cases around the K point and R point, indicating semimetal-insulator transitions. **(g, h)** Such bandgaps are further plotted as the function of ε_x and ε_y, where we use a cross to mark the strain conditions corresponding to panels (e, f).

graphene is

$$H_{\mathrm{BLG}}(\boldsymbol{k}) = \begin{bmatrix} 0 & -tf(\boldsymbol{k}) & 0 & \langle 1,\boldsymbol{R},A|H_{\perp}|2,\boldsymbol{R},B\rangle \\ -tf^{*}(\boldsymbol{k}) & 0 & 0 & 0 \\ 0 & 0 & 0 & -tf(\boldsymbol{k}) \\ \langle 1,\boldsymbol{R},A|H_{\perp}|2,\boldsymbol{R},B\rangle & 0 & -tf^{*}(\boldsymbol{k}) & 0 \end{bmatrix}. \tag{5}$$

For bilayer graphene systems with bi-axial deformation (shown in Figure 1d), we construct a low-energy continuum model that consists of three terms: two single-layer Dirac–Hamiltonian terms that account for the isolated graphene sheets, and a tunneling term that describes hopping between the two layers. Considering only the K points of three closest neighbors, we can get Hamiltonian $H_{\mathrm{SBLG}}(\boldsymbol{k})$ for bilayer-strained graphene as

$$H_{\mathrm{SBLG}}(\boldsymbol{k}) = \begin{bmatrix} H^{\boldsymbol{k}}_{\mathrm{MG}}\left(\frac{\varepsilon_x}{2},\frac{\varepsilon_y}{2}\right) & T_{\boldsymbol{q}_b} & T_{\boldsymbol{q}_{tr}} & T_{\boldsymbol{q}_{tl}} \\ T^{\dagger}_{\boldsymbol{q}_b} & H^{\boldsymbol{k}_b}_{\mathrm{MG}}\left(-\frac{\varepsilon_x}{2},-\frac{\varepsilon_y}{2}\right) & 0 & 0 \\ T^{\dagger}_{\boldsymbol{q}_{tr}} & 0 & H^{\boldsymbol{k}_{tr}}_{\mathrm{MG}}\left(-\frac{\varepsilon_x}{2},-\frac{\varepsilon_y}{2}\right) & 0 \\ T^{\dagger}_{\boldsymbol{q}_{tl}} & 0 & 0 & H^{\boldsymbol{k}_{tl}}_{\mathrm{MG}}\left(-\frac{\varepsilon_x}{2},-\frac{\varepsilon_x}{2}\right) \end{bmatrix}. \tag{6}$$

Here H_{MG} is the Hamiltonian for monolayer graphene, i.e., $H_{\mathrm{SMG}}(\boldsymbol{k})$ for symmetrical and $H_{\mathrm{ASMG}}(\boldsymbol{k})$ for asymmetrical system, T is the tunneling term for interlayer hopping. On basis of the hamiltonian matrix, we further obtain the renormalization of Fermi velocity v_{F}^{*}:

$$\frac{v_{\mathrm{F}}^{*}(\theta)}{v_{\mathrm{F}}} = 1 - \left(\frac{t_{\perp}(K)}{v_{\mathrm{F}}\hbar|\boldsymbol{k}|A_{\mathrm{u.c.}}}\right)^{2} \frac{1}{\sqrt{(\varepsilon_x^2+\varepsilon_y^2)/2}}, \tag{7}$$

where $A_{u.c.}$ is unit cell area, $t_{\perp}(K) = 0.58$ eV Å^2 denotes the interlayer hopping term for Bernal stacked bilayer graphene, V_{F} is the pristine Fermi velocity, and $\hbar$ is the Plank constant. Following Eq. 7, Fermi velocity will decay to zero under small ε_x and ε_y, which potentially generates superconductivtiy. Details of the TBM are presented in the supplementary information [50] (see also references [51, 52] therein).

Results and Discussion

Semimetal-insulator transition in monolayer graphene

To verify the accuracy of the established TBM, we conduct simulations based on first principle calculations of density functional theory (DFT). The results by TBM and DFT simulations show perfect agreement with each other, as shown in Figure 2. In the symmetrical strain conditions ($\varepsilon_x = \varepsilon_y \neq 0$), we observe that the slope of the band structure decreases near the K point, which indicates the decrement of Fermi velocity according to the law $V_{\mathrm{F}} = 2\pi E/(\hbar k)$. In addition, the bandgap is observed to be zero, because the symmetrical strain field retains the geometry symmetry of hexagonal lattices. In the asymmetrical strain conditions ($\varepsilon_x \neq \varepsilon_y \neq 0$), the bandgap will open near the K and R high symmetry points, due to the destruction of geometry symmetry in Hexagonal lattices, as observed in Figure 2e-f. Such a bandgap-opening phenomenon indicates that the monolayer graphene generates semimetal-insulator transitions. Partial enlargement of these band structures are presented as inserts in Figure 2g-h which depicts the general relationship between the bandgap and the strain. Results show that the bandgap will open largely if the monolayer graphene is stretched in one direction while compressed in another direction, i.e., inhomogeneous strain condition $\varepsilon_x\varepsilon_y < 0$. It is also found that the bandgap value increases with the increase of applied strain differences. We get a bandgap of 0.39 eV when strain condition $\varepsilon_x = -10\%, \varepsilon_y = 20\%$ is imposed. This value is much larger than unidirectional stretch or compression obtained in literature [48]. In addition, by releasing homogeneous strain in orthogonal directions (compressive strain only or tensile strain only, $\varepsilon_x\varepsilon_y > 0$), we can still obtain bandgap opening, but smaller than the inhomogeneous strain conditions. This can be intuitively interpreted from the fact that inhomogeneous strain conditions will result in a larger destruction of the geometry symmetry in Hexagonal lattices.

Phonon-mediated superconductivity in bi-layer graphene

We then investigate the band structures of Bernal-stacked bilayer graphene. The influence of interlayer distance is first studied based on TBM and DFT methods. Results in Figure 3a-b show that the valence band and conduction band will get separated respectively when the interlayer distance is $h = 5$ Å. Such a phenomenon is induced by the weak Van der Waals force [53], and this result agrees well with literature [49]. We further reveal the dependence of such separation E_p on the interlayer distance in Figure 3c, here, E_P is the separation value of conduction band at K point. With the increment of interlayer distance, the separation becomes smaller and tends to be negligible when the interlayer distance is larger than 10 Å. In subsequent analysis, we consider bilayer graphene with the interlayer distance $h = 3.45$ Å, which is closer to the interlayer distance of Bernal-stacked graphene [54]. Specifically, we consider deformed bilayer graphene with one layer fixed and another layer stretched or compressed in orthogonal directions ($\varepsilon_{\mathrm{H}} = 11.3\%$), as shown in Figure 3d. The region enclosed by black lines is the unit cell, where $\boldsymbol{a}_1^m$ and $\boldsymbol{a}_2^m$ are the basis vectors, $\boldsymbol{q}_b$, $\boldsymbol{q}_{tr}$ and $\boldsymbol{q}_{tl}$ represent the momentum difference of the K point between the fixed layer and the biaxially stretched layer, as shown in Figure 3e. We consider the K points of the nearest three neighbours in the fixed layer (Figure 3f), their momentum differences to the origin exactly meet the momentum conservation law.

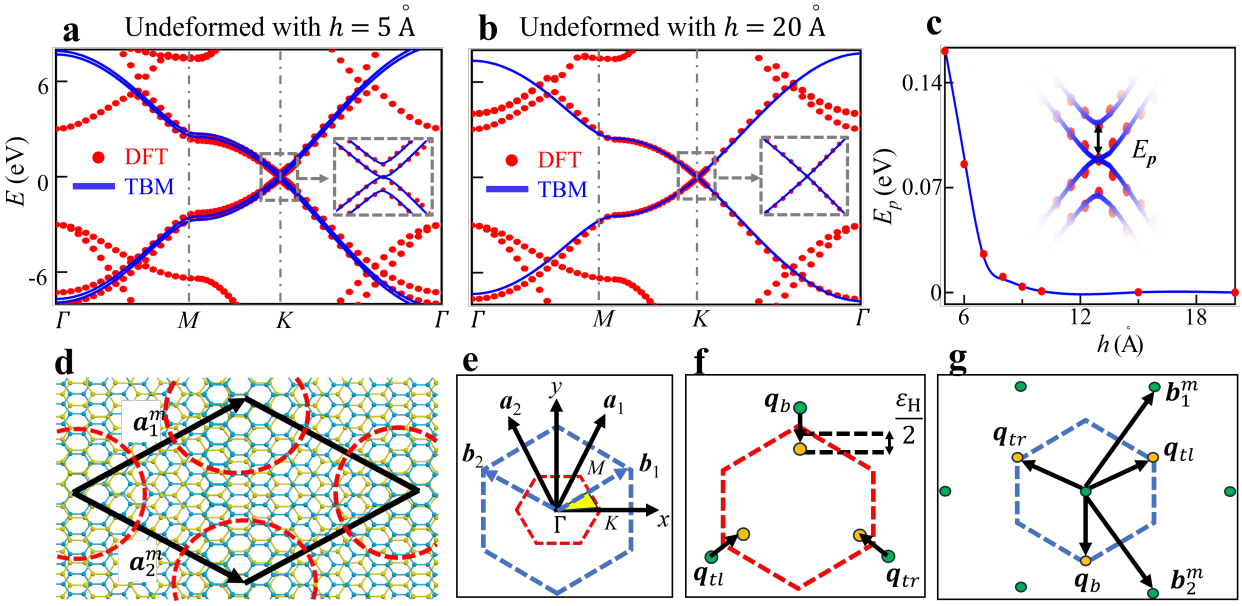

Figure 3: Band structures for Bernal-stacked bilayer graphene with different interlayer distances: **a** $h = 5$ Å; **b** $h = 20$ Å. In panel (a), the inset zoom around the K point shows that the valence band and conduction band are separated from each other due to weak Van der Waals forces, and in panel **(c)**, such separation is further plotted as a function of the interlayer distance h. **(d)** Moiré patterns in symmetrical strained bilayer graphene ($\varepsilon_H = 11.3\%$), where the red circles denote high-energy AA stacking regions and the black diamond shows the potential periodic computational domain. **(e)** Reciprocal lattices and **(f)** momentum-space diagram for the interlayer hopping for symmetrical strained bilayer graphene. The first Brillouin zone is depicted by red lines for the pristine state, and equivalent Dirac points (K and K') are marked by green (orange) dots. **(g)** Three distinct hopping processes in reciprocal space are depicted by $\boldsymbol{q}_b$, $\boldsymbol{q}_{tr}$ and $\boldsymbol{q}_{tl}$. The blue dashed line marks a Moiré unit cell, $\boldsymbol{b}_1^m$ and $\boldsymbol{b}_2^m$ are the basis vectors.

Besides, the K points are staggered due to biaxial stretch, they constitute a new set of honeycomb lattices, thus satisfying the requirements by equation (6).

We compare the TBM and DFT results for bilayer graphene with bi-axial symmetrical deformation ($\varepsilon_x = \varepsilon_y \neq 0$). As compression can easily induce wrinkling of graphene sheets in practical senses [55] and affect the electrical properties, here we only emphasize stretch conditions. Analysis on compression conditions are in the supplementary information [50]. As shown in Figure 4a, theoretical predictions (by TBM) are in good agreement with simulation results (by DFT), verifying the effectiveness of our TBM. Based on the established TBM, we first investigate the band structures of bilayer graphene with different stretch conditions. It is found that the curve slope near the K point decreases gradually with reduced tensile strain, which indicates a growing lower Fermi velocity. In Figure 4c, we show the band structure and density of states near the charge neutrality point calculated for $\varepsilon_{\mathrm{H}} = 1.9\%$. A flat band is observed for the band structure and a peak value appears for the density of states at the Fermi level, which indicates that the Fermi velocity of the electron is zero, i.e., a magic strain in analogy with magic angle is obtained. In this magic-strain case, it is difficult for the electron to hop from the conduction band to the valence band.

We adopt the McMillan formula [56] to obtain the Bardeen–Cooper–Schrieffer (BCS) superconductivity critical temperature as $T_{\mathrm{c}} = \frac{\hbar\omega_{\mathrm{D}}}{1.45 k_{\mathrm{B}}} \exp\left(-\frac{1.04(1+\lambda)}{\lambda-\mu_c^*(1+0.62\lambda)}\right)$, here, λ is a strong BCS coupling strength and is larger than 1, k_{B} is Boltzman constant, $\hbar\omega_{\mathrm{D}}$ is the Debye frequency, and μ_{c}^* is the reduced Coulomb coupling strength. To reveal the dependence of T_{c} on the factor λ, we have to consider s-wave pairing of the bilayer graphene with symmetrical strain. In the s-wave intra-sublattice channel, the local pairing amplitude is expressed as

$$\Delta_l^{(s)}(\boldsymbol{r}) = \left\langle \Psi_{\alpha 1}(\boldsymbol{r})\Psi_{\beta 2}(\boldsymbol{r})\right\rangle = -\left\langle \Psi_{-\alpha 2}(\boldsymbol{r})\Psi_{\beta 1}(\boldsymbol{r})\right\rangle. \tag{8}$$

Here, α_l or β_l denotes different sublattices in different layers l (1 or 2). We assume that the pair amplitude has Moiré periodicity, then we can obtain $\Delta_l^{(s)}(\boldsymbol{r}) = \sum_{\boldsymbol{b}} e^{i\boldsymbol{b}\cdot\boldsymbol{r}}\Delta_{\boldsymbol{b},l}^{(s)}$. Here, $\boldsymbol{b}$ is the Moiré reciprocal lattice vector

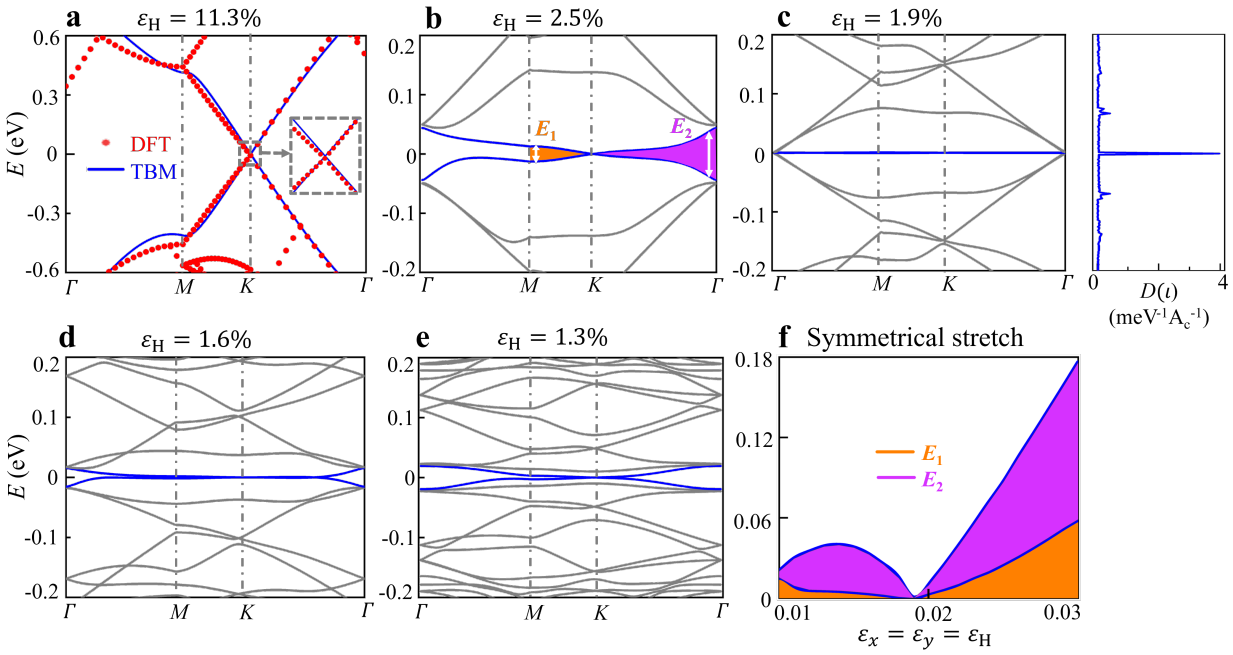

Figure 4: Superconductivity in magic-strain bilayer graphene. Band structures of symmetrical strained bilayer graphene are shown for: **(a)** $\varepsilon_H = 11.3\%$, **(b)** $\varepsilon_H = 2.5\%$, **(c)** $\varepsilon_H = 1.9\%$, **(d)** $\varepsilon_H = 1.6\%$ and **(e)** $\varepsilon_H = 1.3\%$. The inset zoom shows no bandgap around the K point, and the Fermi velocity $V_F = 2\pi E/(\hbar k)$ decreases with inclined stretching strains, as the curve slopes around the K point decrease in the range $\varepsilon_H > 1.9\%$. For strain condition $\varepsilon_H = 1.9\%$ in panel (c), flat band is observed and a peak value appears at the Fermi level, which demonstrates potential superconductivity. E_1 and E_2 are the separation value at M and Γ point respectively, and they are plotted as the function of strain ε_H in panel **f**. The bandgap first gradually decays to zero at $\varepsilon_H = 1.9\%$, then increases beyond this critical value.

of undeformed graphene and follows

$$\begin{aligned}
\Delta^{(s)}_{\boldsymbol{b},l} &= \sum_{\boldsymbol{b}l} \xi^{l_1 l_2}_{\boldsymbol{b}_1 \boldsymbol{b}_2} \Delta^{(s)}_{\boldsymbol{b},l}, \\
\xi^{l_1 l_2}_{\boldsymbol{b}_1 \boldsymbol{b}_2} &= \frac{2g_0}{A} \sum_{\boldsymbol{q},n_1,n_2} \left(\frac{1 - n_F\left[\iota_{n_1}(\boldsymbol{q})\right] - n_F\left[\iota_{n_2}(\boldsymbol{q})\right]}{\iota_{n_1}(\boldsymbol{q}) + \iota_{n_2}(\boldsymbol{q}) - 2\mu} \times \left[\langle u_{n_1}(\boldsymbol{q}) \mid u_{n_2}(\boldsymbol{q}) \rangle_{b_1,l_1} \right]^* \langle u_{n_1}(\boldsymbol{q}) \mid u_{n_2}(\boldsymbol{q}) \rangle_{\boldsymbol{b}_2,l_2} \right),
\end{aligned} \tag{9}$$

where A is the sample area, ξ is the pair susceptibility, $|u_n\rangle$ is the wave function, g_n ($n = 0,1,2$) is the attractive interaction strength whose approximate value $\tilde{g}_0 = g_0 - \sqrt{3}Ua_0^2/4$ is used to evaluate λ as $\lambda = \exp(\tilde{g}_0/g_0)$. Here, U is the on-site repulsion on the honeycomb lattice of each graphene layer and we have the relation $g_0 = g_1 + g_2$, where g_1 and g_2 are taken as 52 meVnm^2 and 69 meVnm^2, respectively [57, 58, 59]. The overlap function $\langle \cdots \rangle_{\boldsymbol{b},l}$ is the layer-resolved matrix element of the plane-wave operator $\exp(i\boldsymbol{b}\cdot\boldsymbol{r})$. Note that $\hat{\mathcal{T}}$ symmetry has been employed in Eq. (9).

The critical temperature T_c is reached when the largest eigenvalue of ξ is equal to 1. In Figure 5, we calculate T_c for $\varepsilon_H = 1.9\%$ including $\boldsymbol{b}$ up to the third Moiré reciprocal lattice vector shell. The largest value of T_c, which exceeds 10 K near the magic strain, can be understood by examining the uniform susceptibility, which has the standard form $g_0 \int d\iota D(\iota)[1 - 2n_F(\iota)]/[2(\iota - \mu)]$. Here $D(\iota)$ is the density of states per spin-valley, $n_F(\iota)$ is the Fermi-Dirac occupation function, μ is the chemical potential, ι is the corresponding energy. Depending on the exact values of λ, s-wave intrasublattice channel can lead superconductivity instability. Note that we did not fulfill the tough task of exactly calculating λ and T_c for our system, but made estimations of T_c on typical λ instead. We aim to demonstrate that the high density of states at the Fermi level will induce a strong phonon-electron coupling which, can cause superconductivity. Such estimations are enough for a proof-of-concept demonstration. See more details in the supplementary information [50]. As a quantitative illustration, we present the relationship between the bandgap at Γ and M points in Figure 4f. It is observed that only under the magic strain $\varepsilon_H = 1.9\%$, the D-value (refers to the difference between

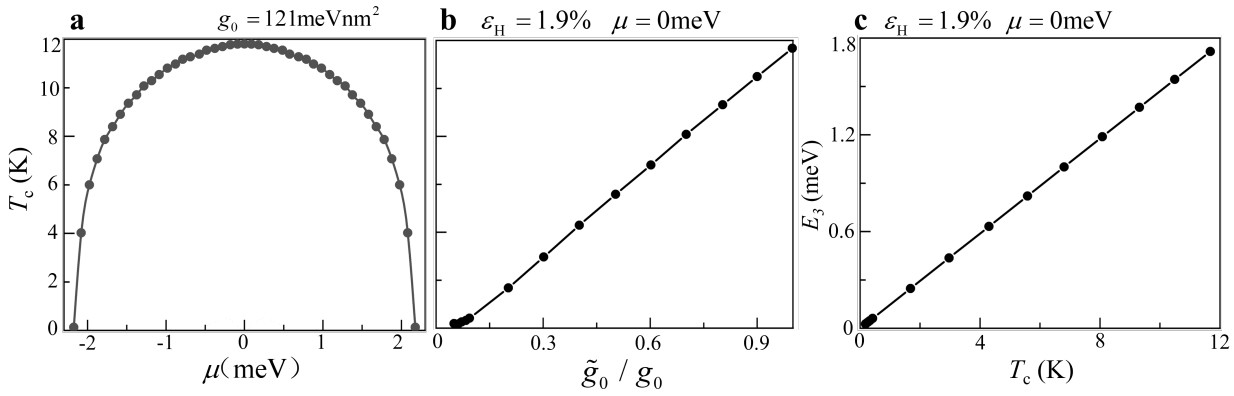

Figure 5: Critical temperature T_c in s-wave as a function of (a) chemical potential μ and (b) reduced attractive interaction strength g_0. (c) Superconducting gap E_3 as a function of T_c. Here, $E_3 = 1.76\, k_B\, T_c$.

E_1 and E_2) approaches zero, as verified by Figure 4c.

We further investigate the bilayer graphene system with bi-axial asymmetrical strains ($\varepsilon_x \neq \varepsilon_y$). It is found that the bandgaps are open only under asymmetrical strain conditions and are closed if symmetrical strains are imposed, as shown in Figure 6a-e. The density of states is shown in the right panel of Figure 6c, where neither peak value nor bandgap are observed. In Figure 6f we show that the bandgap value increases with increased D-value of tensile strain in x and y direction, as a result of increased destruction of geometry symmetry. In the case where $\varepsilon_x = -0.15$ and $\varepsilon_y = 0.15$, the value of bandgap is observed to be 0.0272 eV which is much smaller than its strained monolayer graphene counterpart. Such findings indicate that monolayer graphene is much easier to generate semimetal-insulator transition than bilayer graphene when relaxation strains are imposed. In addition, the bandgap value exhibits different dependency behavior on ε_x and ε_y, which is induced by the chiral properties of graphene.

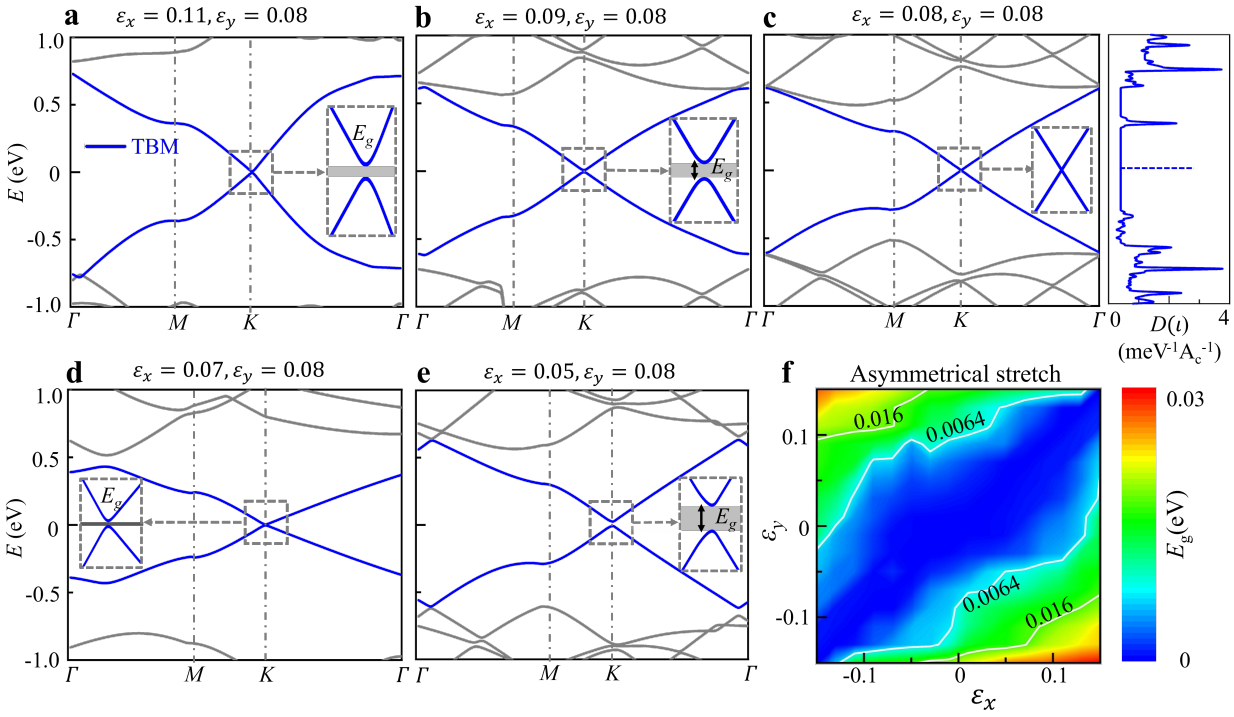

Figure 6: Band structure for asymmetrical strained bilayer graphene: **(a)** $\varepsilon_x = 0.11$; **(b)** $\varepsilon_x = 0.09$; **(c)** $\varepsilon_x = 0.08$; **(d)** $\varepsilon_x = 0.07$; **(e)** $\varepsilon_x = 0.05$, all obtained from TBM. The inset zooms around the K point show bandgaps that indicate semimetal-insulator transitions. **f** Such bandgaps are plot as functions of ε_x and ε_y. The bandgap increases with increasing D-value of ε_x and ε_y.

Conclusion

Summarizing, we have shown that relaxation-strained graphene has the potential to be a superconductor or insulator. Firstly, asymmetrical strain distribution will result in the bandgap opening of monolayer graphene, which indicates that a semimetal-insulator transition is generated. If we impose different types of strain on the monolayer graphene (compressive strain in one direction and tensile strain in another direction, $\varepsilon_x\varepsilon_y < 0$), the bandgap will open largely due to severe destruction of the geometry symmetry in hexagonal lattices. By contrast, if the same types of strain are applied (compression or stretch in both directions, $\varepsilon_x\varepsilon_y > 0$), the bandgap of monolayer graphene is small. In extreme conditions, if the stretch or compression rates in two directions are identical ($\varepsilon_x = \varepsilon_y$), the bandgap will vanish, also the curve slope near the K point will be reduced relative to the pristine graphene, which indicates that stretch or compression will reduce the Fermi velocity. Following these findings, we compression the monolayer graphene by 10% in one direction and stretch it by different rates in another direction. It is found that the bandgap value increases with the increase of strain differences. Specifically, the bandgap can be as large as 0.39 eV on condition of $\varepsilon_x = -10\%, \varepsilon_y = 20\%$, which is much larger than unidirectional stretch or compression ever reported. Secondly, a small interlayer distance will induce separation of the conduction band and valence band from each other due to weak Van der Waals forces, and such separation phenomenon can be eliminated if the interlayer distance is larger than 10Å. Lastly, under the condition that one graphene layer is fixed while another layer is bi-axially stretched (or compressed), the Fermi velocity will decrease with decreasing tensile strains. When the symmetrical strain is at the magic-strain 1.9%, a flat band is generated which indicates that the bilayer graphene turns out to be a superconductor below the critical temperature. By contrast, bi-axially asymmetrical stretched (or compressed) conditions will generate bandgap opening which indicates semimetal-insulator transitions. Generally, we pave a new avenue to achieve graphene superconducting or insulating states by tailoring bi-axial strains. Compared with widely-used twisted systems, the relaxation strain is easier to implement in practice and adds more flexibility to obtain exotic electronic properties by strain engineering.

Theory and calculation

Theoretical model

Considering the situation that one graphene layer is fixed and another layer is stretched in orthogonal directions, the Hamiltonian will consist of two single-layer Dirac–Hamiltonian terms and a tunneling term. In this section, we present the process to simplify the tunneling term. The matrix element for the tunneling term based on the continuum model is

$$T^{\alpha,\beta}_{\boldsymbol{k},\boldsymbol{k}'} = \left\langle \Psi_{\boldsymbol{k},\alpha} \left| H_\perp \right| \Psi^{\varepsilon}_{\boldsymbol{k}',\beta} \right\rangle. \tag{10}$$

Here, the tunneling Hamiltonian $H_\perp$ describes a process during which an electron with momentum $\boldsymbol{k}' = M\boldsymbol{k}$ in the fixed layer hops to the momentum state $\boldsymbol{k}$ in the stretched layer. The left and right vectors are Bloch wave functions

$$\begin{aligned} \left|\psi_{\boldsymbol{k},\alpha}\right\rangle &= \tfrac{1}{\sqrt{N_1N_2}} \textstyle\sum_{n_1,n_2} e^{i\boldsymbol{k}\cdot\left(\boldsymbol{R}_{n_1,n_2}+\boldsymbol{\delta}_\alpha\right)} \left|\boldsymbol{R}_{n_1,n_2}+\boldsymbol{\delta}_\alpha,\alpha\right\rangle, \\ \left|\psi^{\varepsilon}_{\boldsymbol{k}',\beta}\right\rangle &= \tfrac{1}{\sqrt{N_1N_2}} \textstyle\sum_{n_1',n_2'} e^{i\boldsymbol{k}'\cdot\left(\boldsymbol{R}^{\varepsilon}_{n_1',n_2'}+\boldsymbol{\delta}^{\varepsilon}_\beta\right)} \left|\boldsymbol{R}^{\varepsilon}_{n_1',n_2'}+\boldsymbol{\delta}^{\varepsilon}_\beta,\beta\right\rangle. \end{aligned} \tag{11}$$

where the vectors in the deformed layer have all taken into account the tensile strain, and they are set as $\alpha = A, \boldsymbol{\delta}_\alpha = 0$ and $\alpha = B, \boldsymbol{\delta}_\alpha = \boldsymbol{\delta}$. Substituting equation (11) into equation (10), we can obtain

$$\begin{aligned} T^{\alpha,\beta}_{K+\boldsymbol{q}_1,K^\varepsilon+\boldsymbol{q}_2^\varepsilon} &= \tfrac{1}{N_1N_2} \textstyle\sum_{n_1,n_2} \sum_{n_1',n_2'} e^{-i(K+\boldsymbol{q}_1)\cdot\left(\boldsymbol{R}_{n_1,n_2}+\boldsymbol{\delta}_\alpha\right)} e^{i\left(K^\varepsilon+\boldsymbol{q}_2^\varepsilon\right)\cdot\left(\boldsymbol{R}^{\varepsilon}_{n_1',n_2'}+\boldsymbol{\delta}^{\varepsilon}_\beta\right)} \\ &\quad \times \left\langle \boldsymbol{R}_{n_1,n_2}+\boldsymbol{\delta}_\alpha,\alpha \left| H_\perp \right| \boldsymbol{R}^{\varepsilon}_{n_1',n_2'}+\boldsymbol{\delta}^{\varepsilon}_\beta,\beta \right\rangle. \end{aligned}$$

We define the last term as a transition matrix element

$$\left\langle \boldsymbol{R}_{n_1,n_2}+\boldsymbol{\delta}_\alpha,\alpha\left|H_\perp\right|\boldsymbol{R}^{\varepsilon}_{n_1',n_2'}+\boldsymbol{\delta}^{\varepsilon}_\beta,\beta\right\rangle = t_\perp\left(\boldsymbol{R}_{n_1,n_2}+\boldsymbol{\delta}_\alpha-\boldsymbol{R}^{\varepsilon}_{n_1',n_2'}-\boldsymbol{\delta}^{\varepsilon}_\beta\right), \tag{12}$$

and use Fourier transform for simplification

$$\begin{aligned} T^{\alpha,\beta}_{K+\boldsymbol{q}_1,K^\varepsilon+\boldsymbol{q}^\varepsilon_2} = \; & \tfrac{1}{(N_1N_2)^2}\textstyle\sum_{n_1,n_2}\sum_{n_1',n_2'}\sum_{\boldsymbol{k}} e^{i[\boldsymbol{k}-(K+\boldsymbol{q}_1)]\cdot\boldsymbol{R}_{n_1,n_2}}\times e^{i\left[\left(K^\varepsilon+\boldsymbol{q}^\varepsilon_2\right)-\boldsymbol{k}\right]\cdot\boldsymbol{R}^{\varepsilon}_{n_1',n_2'}} \\ & \times e^{i[\boldsymbol{k}-(K+\boldsymbol{q}_1)]\cdot\boldsymbol{\delta}_\alpha+\boldsymbol{\tau}\times e^{i\left[\left(K^\varepsilon+\boldsymbol{q}^\varepsilon_2\right)-\boldsymbol{k}\right]\cdot\left(\boldsymbol{\delta}^{\varepsilon}_\beta-\boldsymbol{\delta}+\boldsymbol{\tau}\right)\frac{t_\perp(K)}{A_{\text{u.c.}}}}}. \end{aligned} \tag{13}$$

We then define reciprocal lattice vectors to simplify equation (13), and transform its form from the real space to the reciprocal space:

$$T^{\alpha,\beta}_{K+\boldsymbol{q}_1,K^\varepsilon+\boldsymbol{q}^\varepsilon_2} = \sum_{k,l,m,n}\frac{t_\perp\left(K+\boldsymbol{q}_1+\boldsymbol{G}_{k,l}\right)}{A_{\text{u.c.}}}e^{i\left[\boldsymbol{G}_{k,l}\cdot\boldsymbol{\delta}_\alpha-\boldsymbol{G}_{m,n}\cdot\left(\boldsymbol{\delta}^{\varepsilon}_\beta-\boldsymbol{\delta}\right)-\boldsymbol{G}^{\varepsilon}_{m,n}\cdot\boldsymbol{\tau}\right]}\delta_{K+\boldsymbol{q}_1+\boldsymbol{G}_{k,l},K^\varepsilon+\boldsymbol{q}^\varepsilon_2+\boldsymbol{G}^{\varepsilon}_{m,n}}. \tag{14}$$

Here, $\boldsymbol{G}$ is summed over reciprocal lattice vectors. The main contribution sum in the formula $T^{\alpha,\beta}_{K+\boldsymbol{q}_1,K^\varepsilon+\boldsymbol{q}^\varepsilon_2}$ originates from $\boldsymbol{G}_{m,n}$, $\boldsymbol{b}^{\varepsilon}_2$ and $-\boldsymbol{b}^{\varepsilon}_1$, hence $K+\boldsymbol{G}^{\varepsilon}_{m,n}$ correspond to three K points. In this manner, $\boldsymbol{q}_1$ and $\boldsymbol{q}^{\varepsilon}_2$, which are close to K and K^ε, can satisfy the momentum conservation law. Substituting the value $\boldsymbol{G}_{m,n}$ into above equations, we then obtain

$$\begin{aligned} T^{\alpha,\beta}_{K+\boldsymbol{q}_1,K^\varepsilon+\boldsymbol{q}^\varepsilon_2} = \; & \tfrac{t_\perp(K)}{A_{u.c.}}\left[\delta_{K+\boldsymbol{q}_1,K^\varepsilon+\boldsymbol{q}^\varepsilon_2}+e^{i\left[\boldsymbol{b}_2.\left(\boldsymbol{\delta}_\alpha-\boldsymbol{\delta}^{\varepsilon}_\beta+\boldsymbol{\delta}\right)-\boldsymbol{b}^{\varepsilon}_2.\boldsymbol{\tau}\right]}\delta_{K+\boldsymbol{q}_1+\boldsymbol{b}_2,K^\varepsilon+\boldsymbol{q}^\varepsilon_2+\boldsymbol{b}^{\varepsilon}_2}\right. \\ & \left.+e^{-i\left[\boldsymbol{b}_1\cdot\left(\boldsymbol{\delta}_\alpha-\boldsymbol{\delta}^{\varepsilon}_\beta+\boldsymbol{\delta}\right)-\boldsymbol{b}^{\varepsilon}_1\cdot\tau\right]}\delta_{K+\boldsymbol{q}_1-\boldsymbol{b}_1,K^\varepsilon+\boldsymbol{q}^\varepsilon_2-\boldsymbol{b}^{\varepsilon}_1}\right]. \end{aligned} \tag{15}$$

Here, all the four possible degrees of freedom for the sublattice are $\{\alpha,\beta\}=\{A,B\}$, $\boldsymbol{\delta}_A=0,\boldsymbol{\delta}_B=\boldsymbol{\delta}$. Then we can write the transition matrix in a two-order form

$$T=\begin{bmatrix} T^{A,A} & T^{A,B} \\ T^{B,A} & T^{B,B}\end{bmatrix}. \tag{16}$$

Thus we can obtain the simplified tunneling term that describes interlayer hopping as

$$T^{\alpha,\beta}_{K+\boldsymbol{q}_1,K^\varepsilon+\boldsymbol{q}^\varepsilon_2} = T_{\boldsymbol{q}_b}\delta_{\boldsymbol{q}^\varepsilon_2-\boldsymbol{q}_1,\boldsymbol{q}_b}+T_{\boldsymbol{q}_{tr}}\delta_{\boldsymbol{q}^\varepsilon_2-\boldsymbol{q}_1,\boldsymbol{q}_{tr}}+T_{\boldsymbol{q}_{tl}}\delta_{\boldsymbol{q}^\varepsilon_2-\boldsymbol{q}_1,\boldsymbol{q}_{tl}}, \tag{17}$$

where $\boldsymbol{\delta}$ is a vector connecting the two atoms in the unit cell, α and β are the sublattice numbers for the fixed layer and stretched layer, respectively. The transition matrices are given by

$$T_{\boldsymbol{q}_b}=\frac{t_\perp(K)}{A_{\text{u.c.}}}\begin{bmatrix}1 & 1\\ 1 & 1\end{bmatrix},$$

$$T_{\boldsymbol{q}_{tr}}=\frac{t_\perp(K)}{A_{u.c.}}e^{-\boldsymbol{b}^m_2\cdot\boldsymbol{\tau}}\begin{bmatrix}e^{-i\theta} & 1\\ e^{i\theta} & e^{-i\theta}\end{bmatrix},$$

$$T_{\boldsymbol{q}_{tl}}=\frac{t_\perp(K)}{A_{\text{u.c.}}}e^{-\boldsymbol{b}^m_1\cdot\boldsymbol{\tau}}\begin{bmatrix}e^{i\theta} & 1\\ e^{-i\theta} & e^{i\theta}\end{bmatrix},$$

where $\boldsymbol{\tau}$ is a translation vector that is almost zero for a small stretch factor, $\boldsymbol{b}^m_1$ and $\boldsymbol{b}^m_2$ are basis vectors for reciprocal lattices shown in Figure 3e. Details on the establishing process of the TBM for different graphene systems are provided in the Supplementary Information [50].

Density Function Theory Calculation

All DFT calculations are conducted using the Vienna Ab initio Simulation package (VASP). The generalized gradient approximation (GGA) and Perdew-Burke Ernzerhof (PBE) function are employed for the exchange-correlation functions. Additionally, the projected augmented wave (PAW) method is utilized to describe the electron interactions. Van der Waals interactions are accounted for using the DFT-D2 method. The truncation energy of plane waves is set to be 550 eV. Structural optimization is considered complete when the force on each atom is less than 0.01 $\text{eV}/\text{Å}$. During the process of structural relaxation, a $5\times5\times1$ K point mesh, based on the Monkhorst-Pack scheme, is employed for geometry optimization. Similarly, a $15\times15\times1$ K-point mesh is used for electronic structure calculations. Different K-point paths are selected based on the specific graphene models under investigation.[50]

Data availability

All the data supporting the conclusions of this study are included in the article and the Supplementary Information file. Data for the figures can be found in the file of Source Data. Source data are provided in this paper.

CRediT authorship contribution statement

Qingxiang Ji: Conceptualization, Formal analysis, Writing original draft. **Bohan Li**: Formal analysis, Methodology, Software. **Johan Christensen**: Methodology, Data curation, Investigation, Review and editing. **Changguo Wang**: Supervision, Validation, Project administration. **Muamer Kadic**: Conceptualization, Supervision, Validation, Review and editing.

Declaration of competing interest

The authors declare that they have no known competing financial interests or personal relationships that could have appeared to influence the work reported in this paper.

Acknowledgements

This work was supported by the National Natural Science Foundation of China [grant numbers 12302169; 12172102]; by the European Union, under Marie Skłodowska-Curie Actions Postdoctoral Fellowships [No. 101149710]; by the French Investissements d'Avenir program, in part by the ANR PNanoBot [ANR-21-CE33-0015] and ANR OPTOBOTS project [ANR-21-CE33-0003]. Computations have been performed on the supercomputer facilities of the Mésocentre de calcul de Franche-Comté.

References

[1] Johan Christensen, Antonio I Fernandez-Dominguez, Fernando de Leon-Perez, Luis Martin-Moreno, and FJ Garcia-Vidal. Collimation of sound assisted by acoustic surface waves. *Nat. Phys.*, 3(12):851–852, 2007.

[2] Kunhao Yu, Nicholas X Fang, Guoliang Huang, and Qiming Wang. Magnetoactive acoustic metamaterials. *Adv. Mater.*, 30(21):1706348, 2018.

[3] Noe Jiménez, Weichun Huang, Vicent Romero García, Vincent Pagneux, and J P Groby. Ultra-thin metamaterial for perfect and quasi-omnidirectional sound absorption. *Appl. Phys. Lett.*, 109(12), 2016.

[4] Robert Schittny, Muamer Kadic, Tiemo Bückmann, and Martin Wegener. Invisibility cloaking in a diffusive light scattering medium. *Science*, 345(6195):427–429, 2014.

[5] Ziwei Wang, Quan Zhang, Kai Zhang, and Gengkai Hu. Tunable digital metamaterial for broadband vibration isolation at low frequency. *Adv. Mater.*, 28(44):9857–9861, 2016.

[6] Robert Schittny, Muamer Kadic, Sebastien Guenneau, and Martin Wegener. Experiments on transformation thermodynamics: molding the flow of heat. *Phys. Rev. Lett.*, 110(19):195901, 2013.

[7] Zhenmin Ding, Xin Li, Qingxiang Ji, Yunce Zhang, Honglin Li, Hulin Zhang, Lorenzo Pattelli, Yao Li, Hongbo Xu, and Jiupeng Zhao. Machine-learning-assisted design of a robust biomimetic radiative cooling metamaterial. *ACS Materials Letters*, 6(6):2416–2424, 2024.

[8] Justyna K Gansel, Michael Thiel, Michael S Rill, Manuel Decker, Klaus Bade, Volker Saile, Georg von Freymann, Stefan Linden, and Martin Wegener. Gold helix photonic metamaterial as broadband circular polarizer. *Science*, 325(5947):1513–1515, 2009.

[9] Muhammad Amin, O Siddiqui, H Abutarboush, Mohamed Farhat, and R Ramzan. A THz graphene metasurface for polarization selective virus sensing. *Carbon*, 176:580–591, 2021.

[10] Muamer Kadic, Graeme W Milton, Martin van Hecke, and Martin Wegener. 3d metamaterials. *Nat. Rev. Phys.*, 1(3):198–210, 2019.

[11] David R Smith, John B Pendry, and Mike CK Wiltshire. Metamaterials and negative refractive index. *Science*, 305(5685):788–792, 2004.

[12] David Schurig, Jack J Mock, BJ Justice, Steven A Cummer, John B Pendry, Anthony F Starr, and David R Smith. Metamaterial electromagnetic cloak at microwave frequencies. *Science*, 314(5801):977–980, 2006.

[13] Andre K Geim and Irina V Grigorieva. Van der Waals heterostructures. *Nature*, 499(7459):419–425, 2013.

[14] K S Novoselov, A Mishchenko, A Carvalho, and AH Castro Neto. 2d materials and van der waals heterostructures. *Science*, 353(6298):aac9439, 2016.

[15] Yuan Meng, Jiangang Feng, Sangmoon Han, Zhihao Xu, Wenbo Mao, Tan Zhang, Justin S Kim, Ilpyo Roh, Yepin Zhao, Dong-Hwan Kim, et al. Photonic van der waals integration from 2d materials to 3d nanomembranes. *Nat. Rev. Mater.*, 8(8):498–517, 2023.

[16] Tao Zhao, Peiyao Xie, Hujie Wan, Tianpeng Ding, Mengqi Liu, Jinlin Xie, Enen Li, Xuequan Chen, Tianwu Wang, Qing Zhang, et al. Ultrathin mxene assemblies approach the intrinsic absorption limit in the 0.5–10 thz band. *Nat. Photonics*, 17(7):622–628, 2023.

[17] Jiazheng Qin, Mengjia Wang, and Cheng Wei Qiu. Graphene metasurface hits the point. *Light Sci. Appl.*, 12(1):110, 2023.

[18] Johan Christensen, Alejandro Manjavacas, Sukosin Thongrattanasiri, Frank HL Koppens, and F Javier García de Abajo. Graphene plasmon waveguiding and hybridization in individual and paired nanoribbons. *ACS nano*, 6(1):431–440, 2012.

[19] LA Ponomarenko, RV Gorbachev, GL Yu, DC Elias, R Jalil, AA Patel, A Mishchenko, AS Mayorov, CR Woods, JR Wallbank, et al. Cloning of dirac fermions in graphene superlattices. *Nature*, 497(7451):594–597, 2013.

[20] Pablo San-Jose, José González, and Francisco Guinea. Non-abelian gauge potentials in graphene bilayers. *Phys. Rev. Lett.*, 108(21):216802, 2012.

[21] Satoru Ichinokura, Katsuaki Sugawara, Akari Takayama, Takashi Takahashi, and Shuji Hasegawa. Superconducting calcium-intercalated bilayer graphene. *ACS Nano*, 10(2):2761–2765, 2016.

[22] F Massee, YK Huang, MS Golden, and M Aprili. Noisy defects in the high-Tc superconductor Bi2sr2cacu2o8+ x. *Nat. Commun.*, 10(1):544, 2019.

[23] Yanzhao Liu, Tianheng Wei, Guanyang He, Yi Zhang, Ziqiang Wang, and Jian Wang. Pair density wave state in a monolayer high-Tc iron-based superconductor. *Nature*, 618(7967):934–939, 2023.

[24] Kyung Hwan Jin, Huaqing Huang, JiaWei Mei, Zheng Liu, Lih King Lim, and Feng Liu. Topological superconducting phase in high-Tc superconductor MgB2 with Dirac–nodal-line fermions. *npj Computational Mater.*, 5(1):57, 2019.

[25] Francisco Guinea, Mikhail I Katsnelson, and AK Geim. Energy gaps and a zero-field quantum hall effect in graphene by strain engineering. *Nat. Phys.*, 6(1):30–33, 2010.

[26] Nikolai N Klimov, Suyong Jung, Shuze Zhu, Teng Li, C Alan Wright, Santiago D Solares, David B Newell, Nikolai B Zhitenev, and Joseph A Stroscio. Electromechanical properties of graphene drumheads. *Science*, 336(6088):1557–1561, 2012.

[27] Jiong Lu, AH Castro Neto, and Kian Ping Loh. Transforming moiré blisters into geometric graphene nano-bubbles. *Nat. Commun.*, 3(1):823, 2012.

[28] Jakob Zabel, Rahul R Nair, Anna Ott, Thanasis Georgiou, Andre K Geim, Kostya S Novoselov, and Cinzia Casiraghi. Raman spectroscopy of graphene and bilayer under biaxial strain: bubbles and balloons. *Nano Lett.*, 12(2):617–621, 2012.

[29] Bruno Amorim, Alberto Cortijo, F De Juan, Adolfo G Grushin, Francisco Guinea, A Gutiérrez-Rubio, Hector Ochoa, Vincenzo Parente, Rafael Roldán, Pablo San-Jose, et al. Novel effects of strains in graphene and other two dimensional materials. *Phys. Rep.*, 617:1–54, 2016.

[30] Jinhai Mao, Slaviša P Milovanović, Miša Anđelković, Xinyuan Lai, Yang Cao, Kenji Watanabe, Takashi Taniguchi, Lucian Covaci, Francois M Peeters, Andre K Geim, et al. Evidence of flat bands and correlated states in buckled graphene superlattices. *Nature*, 584(7820):215–220, 2020.

[31] Zhiwei Li, Yawei Lv, Liwang Ren, Jia Li, Lingan Kong, Yujia Zeng, Quanyang Tao, Ruixia Wu, Huifang Ma, Bei Zhao, et al. Efficient strain modulation of 2D materials via polymer encapsulation. *Nat. Commun.*, 11(1):1151, 2020.

[32] Shengxue Yang, Yujia Chen, and Chengbao Jiang. Strain engineering of two-dimensional materials: methods, properties, and applications. *InfoMat*, 3(4):397–420, 2021.

[33] Md Tareq Mahmud, Dawei Zhai, and Nancy Sandler. Topological flat bands in strained graphene: Substrate engineering and optical control. *Nano Lett.*, 23(16):7725–7732, 2023.

[34] Yuan Cao, Valla Fatemi, Shiang Fang, Kenji Watanabe, Takashi Taniguchi, Efthimios Kaxiras, and Pablo Jarillo-Herrero. Unconventional superconductivity in magic-angle graphene superlattices. *Nature*, 556(7699):43–50, 2018.

[35] Rafi Bistritzer and Allan H MacDonald. Moiré bands in twisted double-layer graphene. *Proc. Natl. Acad. Sci.*, 108(30):12233–12237, 2011.

[36] Grigory Tarnopolsky, Alex Jura Kruchkov, and Ashvin Vishwanath. Origin of magic angles in twisted bilayer graphene. *Phys. Rev. Lett.*, 122(10):106405, 2019.

[37] Cheng Chen, Weichen Tang, Xiang Chen, Zhibo Kang, Shuhan Ding, Kirsty Scott, Siqi Wang, Zhenglu Li, Jacob PC Ruff, Makoto Hashimoto, et al. Anomalous excitonic phase diagram in band-gap-tuned Ta2Ni (Se,S)5. *Nat. Commun.*, 14(1):7512, 2023.

[38] Guangwei Hu, Qingdong Ou, Guangyuan Si, Yingjie Wu, Jing Wu, Zhigao Dai, Alex Krasnok, Yarden Mazor, Qing Zhang, Qiaoliang Bao, et al. Topological polaritons and photonic magic angles in twisted α-MoO3 bilayers. *Nature*, 582(7811):209–213, 2020.

[39] Luis A Gonzalez-Arraga, JL Lado, Francisco Guinea, and Pablo San-Jose. Electrically controllable magnetism in twisted bilayer graphene. *Phys. Rev. Lett.*, 119(10):107201, 2017.

[40] Jeong Min Park, Yuan Cao, Kenji Watanabe, Takashi Taniguchi, and Pablo Jarillo-Herrero. Tunable strongly coupled superconductivity in magic-angle twisted trilayer graphene. *Nature*, 590(7845):249–255, 2021.

[41] Qingxiang Ji, Zhiming Xue, Zaoxu Zhang, Zhanbo Cui, Muamer Kadic, and Changguo Wang. Interlayer torsional sliding and strain localization in bilayer graphene. *Proc. R. Soc. A*, 479(2272):20220833, 2023.

[42] Vahid Morovati, Zhiming Xue, Kenneth M Liechti, and Rui Huang. Interlayer coupling and strain localization in small-twist-angle graphene flakes. *Extreme Mechanics Letters*, 55:101829, 2022.

[43] Riju Banerjee, Viet-Hung Nguyen, Tomotaroh Granzier-Nakajima, Lavish Pabbi, Aurelien Lherbier, Anna Ruth Binion, Jean-Christophe Charlier, Mauricio Terrones, and Eric William Hudson. Strain modulated superlattices in graphene. *Nano Lett.*, 20(5):3113–3121, 2020.

[44] Bjarke S Jessen, Lene Gammelgaard, Morten R Thomsen, David MA Mackenzie, Joachim D Thomsen, José M Caridad, Emil Duegaard, Kenji Watanabe, Takashi Taniguchi, Timothy J Booth, et al. Lithographic band structure engineering of graphene. *Nat. Nanotechnol.*, 14(4):340–346, 2019.

[45] Francisco Guinea and Niels R Walet. Electrostatic effects, band distortions, and superconductivity in twisted graphene bilayers. *Proc. Natl. Acad. Sci.*, 115(52):13174–13179, 2018.

[46] Naoto Nakatsuji and Mikito Koshino. Moiré disorder effect in twisted bilayer graphene. *Phys. Rev. B*, 105(24):245408, 2022.

[47] Zhen Zhang, Lu Wen, Youkai Qiao, and Zhiqiang Li. Effects of strain on the flat band in twisted bilayer graphene. *Chinese Phys. B*, 32(10):107302, 2023.

[48] Jen Hsien Wong, Bi Ru Wu, and Ming Fa Lin. Strain effect on the electronic properties of single layer and bilayer graphene. *J. Phys. Chem. C*, 116(14):8271–8277, 2012.

[49] Gonçalo Catarina, Bruno Amorim, Eduardo V Castro, JMVP Lopes, and Nuno Peres. Twisted bilayer graphene: low-energy physics, electronic and optical properties. *Handbook of Graphene*, 3:177–232, 2019.

[50] See Supplemental Material at [URL] for the tight binding model and charge density of strained graphene. The supplemental material alsocontains refs. [51,52].

[51] Alexandr Vladimirovich Rozhkov, AO Sboychakov, AL Rakhmanov, and Franco Nori. Electronic properties of graphene-based bilayer systems. *Physics Reports*, 648:1–104, 2016.

[52] S Das Sarma and EH Hwang. Collective modes of the massless dirac plasma. *Physical review letters*, 102(20):206412, 2009.

[53] M Van der Donck, FM Peeters, and B Van Duppen. Transport properties of bilayer graphene in a strong in-plane magnetic field. *Physical Review B*, 93(11):115423, 2016.

[54] X Chang, Y Ge, and JM Dong. Ripples of aa and ab stacking bilayer graphenes. *The European Physical Journal B*, 78:103–109, 2010.

[55] Ch Androulidakis, EN Koukaras, MG Pastore Carbone, M Hadjinicolaou, and C Galiotis. Wrinkling formation in simply-supported graphenes under tension and compression loadings. *Nanoscale*, 9(46):18180–18188, 2017.

[56] WL McMillan. Transition temperature of strong-coupled superconductors. *Physical Review*, 167(2):331, 1968.

[57] RM Ribeiro, Vitor M Pereira, NMR Peres, PR Briddon, and AH Castro Neto. Strained graphene: tight-binding and density functional calculations. *New Journal of Physics*, 11(11):115002, 2009.

[58] Bitan Roy, Jay D Sau, and S Das Sarma. Migdal's theorem and electron-phonon vertex corrections in dirac materials. *Physical Review B*, 89(16):165119, 2014.

[59] TO Wehling, E Şaşıoğlu, C Friedrich, AI Lichtenstein, MI Katsnelson, and S Blügel. Strength of effective coulomb interactions in graphene and graphite. *Physical review letters*, 106(23):236805, 2011.